

# Evaluation of On-Vehicle Bone-Conduct Acoustic Emission Detection for Rail Defects

Lei Jia<sup>1</sup>, Jee Woong Park<sup>1</sup>, Ming Zhu<sup>2</sup>, Yingtao Jiang<sup>2</sup>, Hualiang Teng<sup>1</sup>

<sup>1</sup>Department of Civil and Environmental Engineering and Construction, University of Nevada, Las Vegas, NV, USA

<sup>2</sup>Department of Electrical and Computer Engineering, University of Nevada, Las Vegas, NV, USA

Email: [jjal5@unlv.nevada.edu](mailto:jjal5@unlv.nevada.edu), [jee.park@unlv.edu](mailto:jee.park@unlv.edu), [ming.zhu@unlv.edu](mailto:ming.zhu@unlv.edu), [yingtao.jiang@unlv.edu](mailto:yingtao.jiang@unlv.edu), [hualiang.teng@unlv.edu](mailto:hualiang.teng@unlv.edu)

**How to cite this paper:** Jia, L., Park, J.W., Zhu, M., Jiang, Y.T. and Teng, H.L. (2025) Evaluation of On-Vehicle Bone-Conduct Acoustic Emission Detection for Rail Defects. *Journal of Transportation Technologies*, 15, 95-121.

<https://doi.org/10.4236/jtts.2025.151006>

**Received:** November 23, 2024

**Accepted:** January 13, 2025

**Published:** January 16, 2025

Copyright © 2025 by author(s) and Scientific Research Publishing Inc. This work is licensed under the Creative Commons Attribution International License (CC BY 4.0).

<http://creativecommons.org/licenses/by/4.0/>



Open Access

## Abstract

Rail defects can pose significant safety risks in railway operations, raising the need for effective detection methods. Acoustic Emission (AE) technology has shown promise for identifying and monitoring these defects, and this study evaluates an advanced on-vehicle AE detection approach using bone-conduct sensors—a solution to improve upon previous AE methods of using on-rail sensor installations, which required extensive, costly on-rail sensor networks with limited effectiveness. In response to these challenges, the study specifically explored bone-conduct sensors mounted directly on the vehicle rather than rails by evaluating AE signals generated by the interaction between rails and the train's wheels while in motion. In this research, a prototype detection system was developed and tested through initial trials at the Nevada Railroad Museum using a track with pre-damaged welding defects. Further testing was conducted at the Transportation Technology Center Inc. (rebranded as MxV Rail) in Colorado, where the system's performance was evaluated across various defect types and train speeds. The results indicated that bone-conduct sensors were insufficient for detecting AE signals when mounted on moving vehicles. These findings highlight the limitations of contact-based methods in real-world applications and indicate the need for exploring improved, non-contact approaches.

## Keywords

Railroad Infrastructure, Rail Defect Detection, Rail Health Monitoring, Wavelet Analysis, Acoustic Emission Detection

## 1. Introduction

In railroad transportation, the rail and wheels directly interact as trains move forward. The railroads would experience wear and tear during daily operations, lead-

ing to defects both within the rail's internal structure and on its surface. While exterior defects are visible and can be detected using various detection techniques (e.g., vision-based detection), internal defects are hidden and thus require more advanced detection techniques to assess changes in the rails' mechanical and material properties of the rails. To address the challenges of rail defects and ensure the continued safe and reliable operation of railroads, various inspection and monitoring technologies have been developed to assess rail health. Imaging and ultrasound detection techniques have been applied to monitor rail health conditions against rail defects. In addition, some unique methods, such as electromagnetic tomography technology, have been proposed for addressing specific detection problems.

### **1.1. Rail Defect Inspection Technologies**

The optical imaging method is a recognition technology that uses graphics scanning and processing. The core component of this testing system is a high-speed, high-resolution camera. An optical encoder is used for graphics recognition and classification. Recent experimental research has demonstrated surface defect detection at speeds over 135 mph [1]. An automatic optical detecting system can detect flaws using color line-scan cameras and a spectral image differencing procedure [2]. This system is particularly advantageous for detecting minor defects, including invisible cracks. Also, the employment of the system enables automation of about 95% of the inspection work, significantly increasing the efficiency of inspection compared to previous techniques. However, the system is limited to only inline checking of new rails. Advances in software for optical detection have been made. A new algorithm filters the image background through wavelet transformation [3] [4].

Advanced optical technologies include a 3D laser profiling system (3D-LPS) [5]. The system contains a laser scanner, odometer, inertial measurement unit (IMU), and GPS to collect the rail surface information. The results showed that the algorithm could recognize the surface defect and locate the defect area with a relatively good recognition rate. However, the whole experiment was performed in limited setting at approximately 3.4 mph; thus, further research on the application at higher speeds is necessary for more rigorous validation. While research has improved the optical detection system, several problems still exist, limiting system-wide implementation. The primary challenges stem from complex disturbance factors, limited recognition features, and limited capability to detect internal defects [6].

Another inspection technique utilizes ultrasonic without having the sensor make direct contact with the material being inspected. While NCU technology is widely used in structure health inspections, past research [7] employed pulse-echo for rail scanning with an excitation frequency of approximately 200 kHz. The frequency provided a suitable surface wave mode and sufficient penetration depth for inspection. Concurrently, a spatial averaging technique was employed to re-

move unusable wave modes and reduce signal complexity. The results demonstrated that the technology worked well on artificial and real defects. Despite these findings, the research suffers a critical limitation with the very low speeds in static conditions, a common drawback of ultrasonic detection methods.

Guided-wave defect detection in rails has also been applied for non-contact testing, and a prototype is under development [8]. Research has shown that high-frequency waves of approximately 200 kHz are dominant. The penetration depth is related to the wavelength; hence, defect sizing is possible by monitoring different frequency bands of the propagating waves. The researchers at the University of California at San Diego (UCSD) developed a novel non-contact ultrasonic rail inspection system [9]. The new system employs a focused air-coupled transmitter, symmetrically placed air-coupled receivers, and a novel statistical algorithm to maximize true outliers (defects) and minimize false positives. Results demonstrate excellent performance at low speeds between 1 and 5 mph and show promise at speeds of 10 and 15 mph.

Laser ultrasonics was proposed as another non-contact detection technique. The laser ultrasonic system employed an Nd-Yag pulse laser for ultrasonic wave generation and a laser Doppler vibrometer for signal measurement [10]. This study presented the adaptability of laser ultrasonics in defect characterization, with the transformation of the laser beam's shape to cater to different defect types—a line source for surface damage and a point source for internal defects. This method underscores the interaction of ultrasonic waves with defects, enabling the detection of both surface and subsurface anomalies at high speeds.

A passive extraction method has been used to isolate defect signals based on non-contact ultrasonic monitoring [11]. Three options were listed to present the differences in isolating the defect signal: cross-correlation, normalized cross-correlation, and deconvolution. According to previous research, ultrasonic energy and properties will change due to the rails' discontinuities [12] [13]. A defect inspection prototype was developed in the experiment, placing two arrays of air-coupled receivers to collect ultrasonic waves. Normalized cross-correlation and deconvolution operations were used to extract the defect properties during the data analysis. In their discussion, rail lubrication is an uncertain factor that may affect the wheel-rail contact behavior. Meanwhile, many improvements need to be made to increase detection accuracy and faster data analysis.

## 1.2. AE Techniques and Its Applications

AE is an elastic wave generated by changes in the material's internal structure, which are typically caused by a sudden change in internal stress or external impact [14] [15]. These changes can include crack growth in the body, sectional displacement in material, phase change, fiber breakage, and decomposition.

An AE testing system that can be used for detection of such changes contains bone-conduct sensors, preamplifiers, and a data acquisition (DAQ) system (e.g., control software, data recording devices, and personal computers). When AE sig-

nals are generated due to elastic deformation, sensors respond to the dynamic motion and collect the signals. However, these signals can be too weak to effectively present the AE patterns. In response to this, preamplifiers are used to filter interference signals. The frequency of collected AE signals is generally between 20 KHz and 1 MHz; a high-pass filter is applied to filter out the ambient noise. After the noise filtering, the signals are transferred to the AE processing equipment for analysis and storage. During signal processing, the signal goes through a measurement circuit that compares the conditioned signals with a threshold voltage value previously programmed. Finally, the signal is recorded into the storage device.

AE technology differs from other non-destructive testing technologies in several aspects [14] [16]. First, the origin of the signal is different. Instead of providing energy to the object during the examination, AE technology receives the energy released by the material. Second, AE technology only responds to dynamic processes or changes in material. Dynamic response is critical because it can be used to trace the continuous changes in the material. Through the initial research on AE technology, advantages have been presented, such as the ability to detect rail defects at speeds over 100 mph, easy installation and manipulation, and the ability to monitor internal structural changes [14] [17] [18].

In summary, traditional AE techniques present the potential to monitor rail health conditions passively. This potential can be understood in several terms: the capability of detecting both internal and external defects, the potential to monitor the development progress of defects, and the classification of defect types. However, due to the utilization of bone-conduct sensors, such an approach can only be installed on the rails due to the requirement of contact. This installation requirement for contact is translated into an extensive network of sensors to cover the whole rail track where inspection is required. While technically promising, this technique can be practically unfeasible.

## 2. Objective

Past research on the application of AE techniques for detecting damage in railway tracks has primarily focused on lab tests and rail-mounted field experiments. These studies include fatigue tests of rail steel specimen experiments with small-scale models to simulate the wheel-rail impacts, with AE sensors installed on the rails to collect AE signals as trains pass by. However, these approaches have limitedly demonstrated potential for real-world applications due to several constraints. A notable one is the requirement of an extensive network of sensors along the entire length of the railway, which poses significant challenges for real-world implementation.

To address these limitations, this research explored a vehicle-mounted AE approach. The work conducted and presented in this research is essential as it rigorously evaluates an AE technique given its potential identified by past research. The research has taken this approach to a full-scale test in various real-world scenarios for comprehensive evaluation of its feasibility for automated rail health monitor-

ing in operational environments.

### 3. Methodology

This research builds on previous studies, identifying AE technology as a promising solution for detecting internal defects in rail. AE technology can be implemented using bone-conduct sensors for rail inspection. The project explores these sensors by 1) conducting lab tests, small-scale rail-train tests, and full-scale real-world rail-train tests, and 2) performing analytical studies using various algorithmic techniques to analyze AE signals associated with defects. In this research, bone-conduct sensors are mounted on running trains to detect rail defects. This involves an investigation on the characteristics of the rail defect-induced AE signals for defect identification and evaluation of the AE characteristics alongside identification algorithms. The conclusion of the study will reveal insights into the feasibility, performance, and potential limitations of a bone-conduct sensor-based detection system for automated railroad safety inspections.

#### 3.1. On-Vehicle AE Detection Prototype

The prototype developed included data acquisition equipment, bone-conduct sensors, pre-amplifiers, and high-speed cameras (**Figure 1**). Three identical AE sensors S9215 were used, operating within a 50 - 650 KHz bandwidth and a resonant frequency of 100 kHz. They offer a high limit up to 540 °C, allowing adequate testing in the extreme summer weather conditions in Nevada. A National Instrumental cRio 9041 with module NI 9223 were utilized as DAQ equipment with the sampling rate of 1 MHz. Mistras 2/4/6 voltage preamplifiers were employed to amplify AE signals prior to recording by the DAQ system. The preamplifiers' gain was set to 60 dB and a 20 - 500 kHz bandwidth was used to minimize low-frequency noises during the test. LabVIEW was used to manage the data collection and storage. A go-pro camera set at 240 fps recording recorded geo-information during the field tests. Hammer hit was employed when each test started to sync the time between video and AE signals.



**Figure 1.** AE detection prototype.

## 3.2. Test Lay-Out and Procedure

### 3.2.1. Field Test in Nevada Railroad Museum

To assess the feasibility of using the AE sensors mounted on trains to detect rail defects, on-vehicle field tests were conducted in the Nevada Railroad Museum. One rail section containing two pre-damaged internal defects (**Figure 2**) was selected. Approximately 100 feet of track was replaced to include these defects. The sensors were installed on the vehicle to collect AE signals as the train ran over the defect locations.

The used track was an AREMA 130-lb rail with internal defective welds characterized by the crack types and locations. As shown in **Figure 2**, the size of the first defect was 0.2 inches by 0.3 inches, located 0.7 inches below the rail surface. The second defect measured 0.2 inches by 0.2 inches, located 1 inch below the rail surface. Both defects were evaluated by an Olympus Epoch 1000i ultrasonic inspector to be in the early stages of defect development based on size. The rail track was supported by wood sleepers and ballast. The rail gauge was 4 feet 8.5 inches, and the sleeper spacing was about 19 inches.

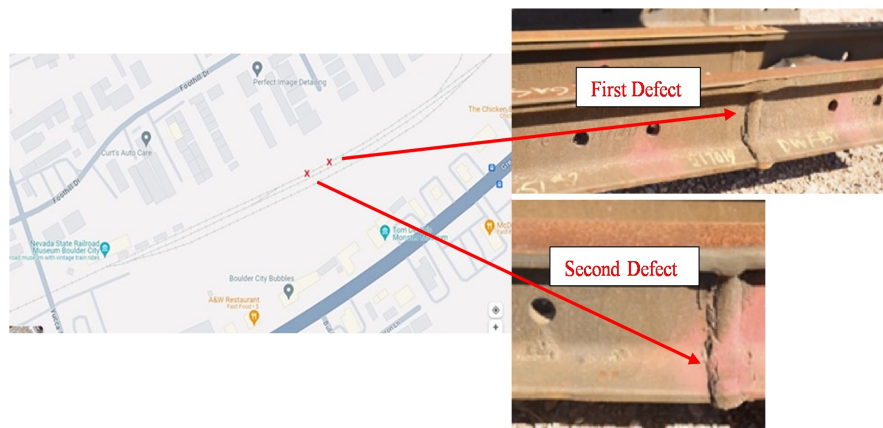


**Figure 2.** Two internal defects and their locations (red x-marked).

Three identical AE sensors were mounted on a steel plate attached to the rail suspension frame (**Figure 3(a)**). This location was selected as it is optimal for collecting AE signals generated by wheel-rail impacts. Ultrasonic coupling gel was applied to ensure signal transmission, and a GoPro camera was installed on the back of the steel plate to record the track geo-information. The DAQ equipment and laptop were placed on the platform above the bogie (**Figure 3(b)**).

Acoustic signals were recorded as a 30-ton empty hopper moved back and forth over the defect locations at about 5 mph. As explained before, a hammer strike was used for synchronization of data between the camera and DAQ equipment at the start of each test. The field tests were conducted in four sets with five runs per set (back and forth as one run). Due to time-restricted access to the test site, the tests were conducted during specific scheduled time slots.

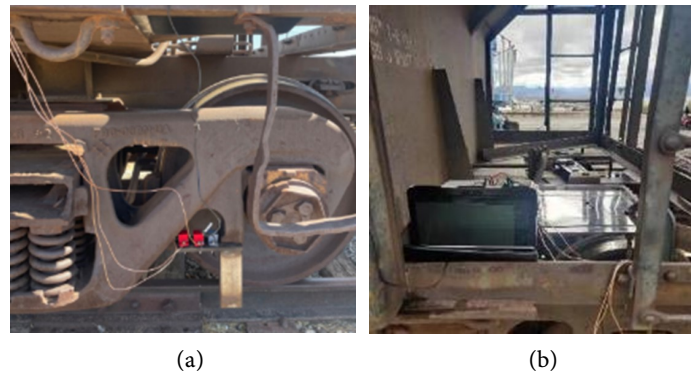


**Figure 3.** Prototype installation.

### 3.2.2. Field Test in TTCI

The defects used at the Nevada Railroad Museum were inside the joint bars, known to produce AE signals that can mimic those generated by rail defects. To mitigate the influence of such confounding factors, further evaluations in a controlled and specialized testing facility are essential. Therefore, a series of field tests were designed and conducted at the TTCI, involving three different loops to vary factors, such as defect quantity and types, axial load, and testing speed. Testing in differently conditioned loops was critical to rigorously assess the system performance in defect detection.

Three tested loops were the Rail Defect Test Facility (RDTF), the High Tonnage Loop (HTL), and the Railroad Test Track (RTT). The RDTF (**Figure 4**) contains over 300 known artificial rail defects. It included a System Evaluation Zone, which spans 4,000 feet and contains over 250 defects with known locations, and a System Calibration Zone, which had approximately 30 defects distributed in dense clusters. Additionally, there was a Blind Zone, which contained various defects with unknown locations and characteristics, designed for verification purposes.

It is important to note that artificial defects like ones in the RDTF might not generate AE signals in the same way natural defects do due to inherent differences in how defects are generated. Analysis of defects whether it is natural or artificial should account for these potential differences in a careful examination. A high-rail vehicle (**Figure 4**), used in the RDTF test, produced an axial load significantly lower than that of real train cars. The low axial load used in testing does not fully replicate real-world scenarios, as commercial railcars typically have much higher weights.

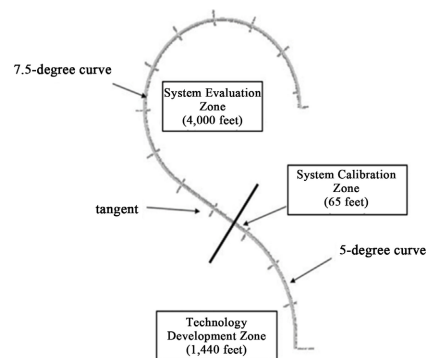




Figure 4. RDTF loop and used hi-rail vehicle in RDTF.

Consequently, additional field tests were designed on the HTL (Figure 5) to verify the system’s performance under a broader range of load scenarios, ensuring a comprehensive evaluation. It is approximately 6.4 miles in length and includes over 30 naturally generated rail defects. The heavy-duty hoppers were utilized for these tests, with a speed limit of 40 mph. The final evaluation test was conducted on the RTT (Figure 5), which is 13.5 miles long with a speed limit of 105 mph. No defect information was provided for this loop; instead, the algorithms developed during the earlier tests were employed to identify defects on the RTT.

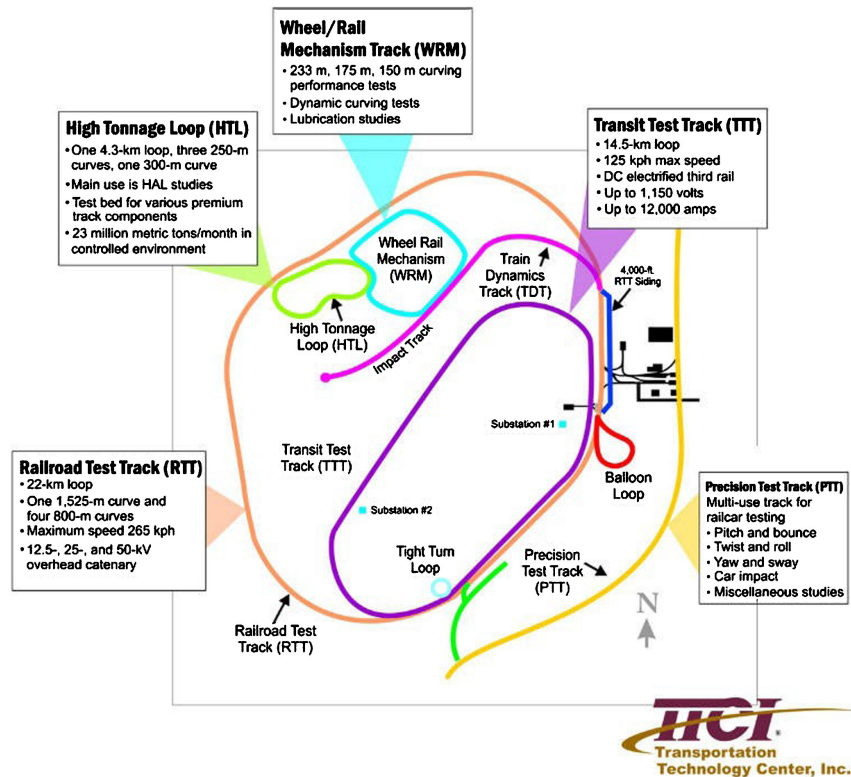


Figure 5. HTL and RTT loops.

**Test Setup in RDTF:** Defects in RDTF were artificially created by cutting or drilling the tracks, as shown in Figure 6. Three identical AE sensors and two Go-Pro cameras were mounted on a steel plate mounted on the bottom frame of the Hi-rail vehicle (Figure 7). The mount locations were carefully selected to ensure

safety and the detectability of AE signals generated by wheel-rail impacts. Ultrasonic coupling gel was applied to the sensor surfaces to ensure effective signal transmission between the sensors and the steel plates. The DAQ equipment and a laptop were housed inside the vehicle.

Acoustic signals were collected as the Hi-rail vehicle, weighing 5 tones, traversed the defects. The same hammer hit was used for data synchronization. Field tests were conducted at four different speeds—5 mph, 10 mph, 15 mph, and 20 mph. The 20-mph setup included 10 runs (each run consisting of a back-and-forth motion), while the other setups had 5 runs each. This ensured sufficient rail-wheel impacts to generate AE events. These tests aimed to collect AE signals at various speeds, enabling a comprehensive evaluation of AE features based on different defect types and vehicle speeds.



**Figure 6.** Defects in RDTF loop.



**Figure 7.** Prototype installation on hi-rail vehicle.

**Test Setup in HTL.** The HTL loop field tests are different as this loop involves naturally created rail defects. It had 39 defects over a loop span of 6.4 miles. As an example, a typical web crack defect is shown in **Figure 8**. For accurate assessment of rail defects, a preliminary inspection was conducted on all defects, one at a time to identify the size, type, and location of each defect. The results were documented by TTCI. Eight defects were located on the bypass track (zone marked by the red area) and thus were excluded from this field testing (**Figure 8**). Therefore, 31 defects distributed on the main loop were used for data collection and further analysis. The vehicle used in this field test was a 30-ton empty hopper (**Figure 9**). The sensors and cameras were installed in the same configuration as in the RDTF tests, and the DAQ equipment was securely placed on top of the bogie.

Three tests were conducted at 20 mph, and ten tests were conducted at 40 mph,

the maximum speed allowed on the HTL loop. The 20-mph tests were designed to collect AE signals with relatively low ambient noise, serving as a baseline or “ground truth” for comparison with the 40-mph tests. The AE signals collected during this phase were later compared with those obtained from the previous tests involving artificially induced defects, highlighting differences between natural and artificial defects. Additionally, AE signals and ambient noises from both field test sets were extracted and used to train machine learning (ML) models to distinguish defects from ambient noise and classify different defect types.

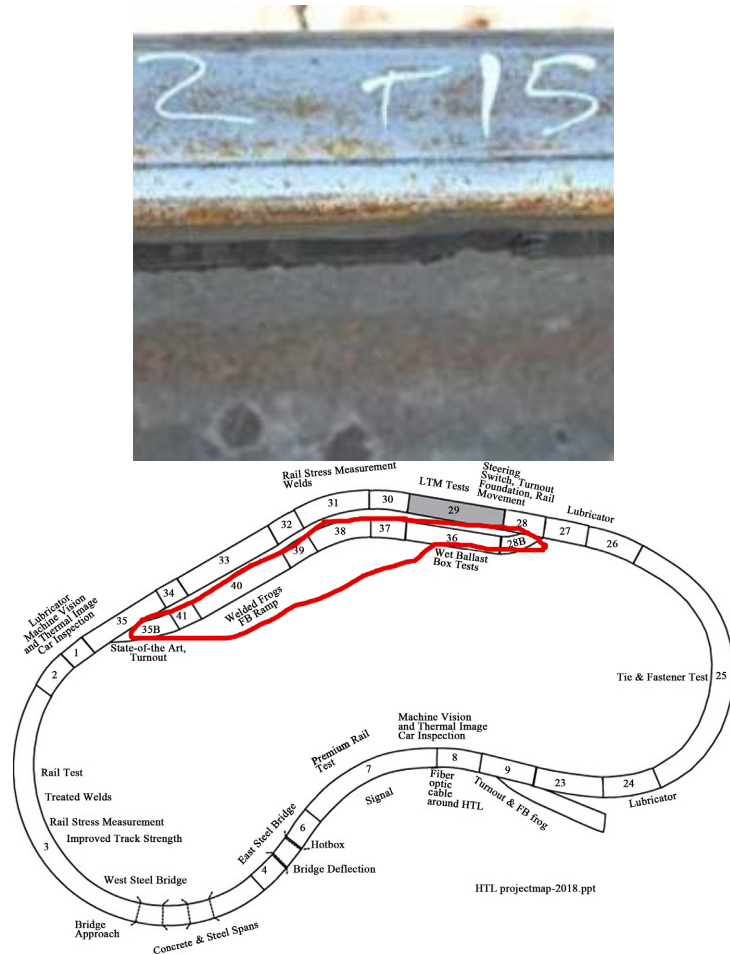


Figure 8. Rail defect and HTL loop.



Figure 9. Testing vehicle and prototype installation on HTL loop.

**Test Setup in RTT.** After completing the tests in the RDTF and HTL loops, AE signals were collected with detailed information and precise defect locations, providing a foundational dataset for model training. Unlike the RDTF and HTL, the RTT loop was designed to include defects without their identified information. That is, their locations and sizes are unknown to the research team. This sequence of tests—RDTF, HTL, and RTT—was intentionally structured to allow the research team to utilize advanced ML techniques for studying rail defects. The data from RDTF and HTL serves as the training data while the data from RTT is used to make predictions of defects captured during high-speed rail operation. These field tests collectively designed with three real-world loops offer a unique testing environment to validate the system’s predictive capabilities under real-world scenarios. This approach ensures that the ML models are both trained on reliable data and validated in scenarios that closely mimic operational challenges. These field tests collectively designed with three real-world loops offer a unique testing environment to validate the system’s predictive capabilities under real-world scenarios.

The entire length of the RTT loop was 13.5 miles, with a maximum allowable speed of 165 mph. The testing system was installed similarly as installed in the Nevada field test, as presented in **Figure 10**. However, due to safety concerns regarding the sensors and cameras, the maximum speed during this test was limited to 105 mph. Five tests were conducted: two at 40 mph and three at 105 mph. The purpose of the 40 mph tests was to evaluate and compare the effects of ambient noise with those observed during the HTL tests.

Key information of the field tests was summarized in **Table 1**. These tests were systematically conducted, with multiple runs at each speed, to ensure robust data collection for subsequent analysis and model training.



**Figure 10.** Testing car and sensor installation on RTT Loop.

**Table 1.** Summary of field tests in TTCL.

Test Location	Length (miles)	Defect Amount	Test Speed (MPH)	Number of Runs	Goal
RDTF	1.04	$\geq 280$	5	5	Evaluate AE features at various speeds
			10	5	
			15	5	
			20	10	
HTL	6.4	39	20	3	Explore and ML models
			40	10	

Continued

			40	2	Evaluate ML
RTT	13.5	Unknown	105	3	model at high speed

## 4. Data Analysis

### 4.1. Time-Frequency Analysis of Nevada Railroad Museum Test

The time-frequency characteristics of AE signals collected in the field tests were processed using Continuous Wavelet Transform (CWT). Due to the early stage of the defect development for both defects, only three AE events were detected during the entire test. Two events were collected from the first defect and one from the second defect.

To effectively present the AE features, a high-pass filter with 60 kHz was employed to reduce the effects of low-frequency noises. **Figure 11** indicated that the wave energy was primarily concentrated in the 60 - 120 kHz and a notable amount of energy was in the 200 - 300 kHz range. In contrast, **Figure 12** presented the CWT of two typical ambient noises, where the energy was mainly concentrated below 150 kHz. This is significantly different from the defect-induced AE signals. Therefore, filtering out the lower frequency components of the AE signal can significantly reduce the impact of noise. Additionally, these visible differences made identifying and canceling ambient noise possible in the future.

The field test in the Nevada Railroad Museum provided a promising result that AE signals caused by rail defect development could be detected and recognized. Meanwhile, general ambient noises presented significantly different characteristics from the AE signals. However, due to the existence of joint bar which can also generate noises affecting the detection of defect signals, further analysis of the field tests from TTCI was presented in the following chapters.

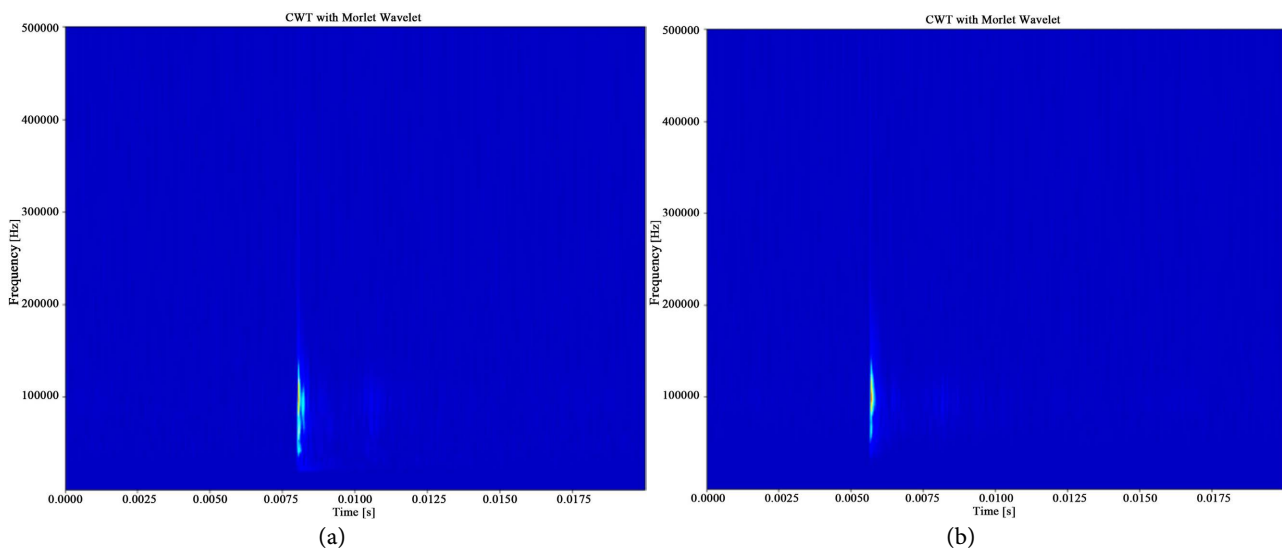


**Figure 11.** Defect-induced AE signals: (a) single impulse; (b) dual impulses.

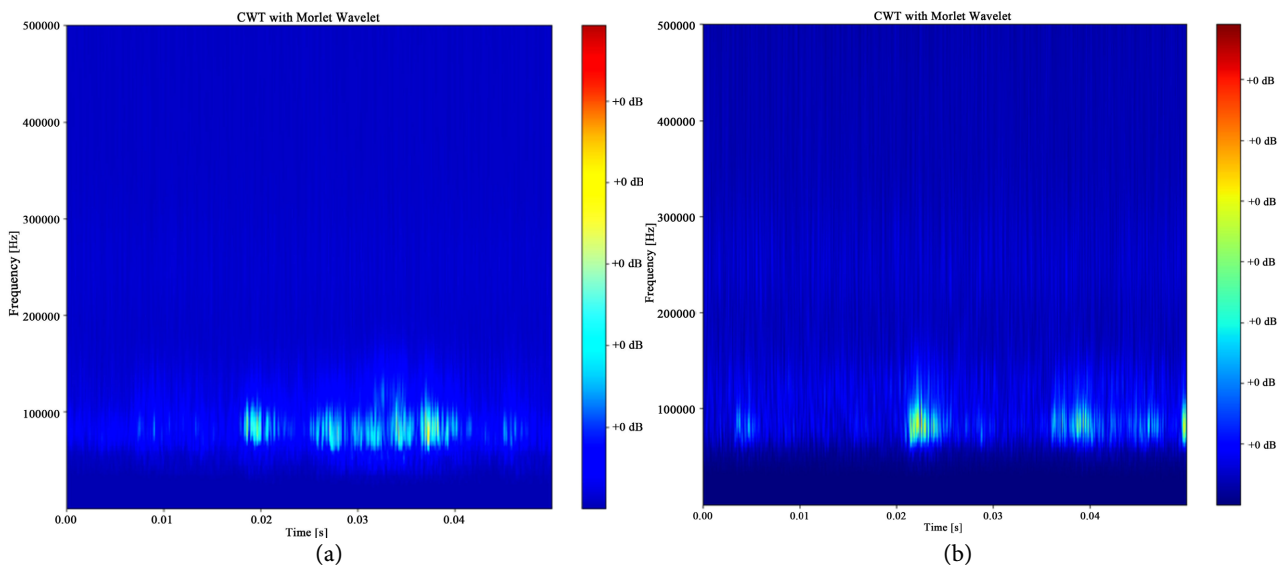


**Figure 12.** Ambient noise-induced signals: (a) braking noise; (b) mechanical vibration.

#### 4.2. Time-Frequency Analysis of RDTF Loop in TTCI

Following the preliminary data analysis of the tests conducted at the Nevada Railroad Museum, the CWT analysis was performed to evaluate the AE characteristics of naturally generated defects on RDTF. A 20 kHz high-pass filter was applied in this test to mitigate the impact of low-frequency noise. Preliminary CWT analysis was conducted using a 0.05-second time window, a duration chosen to balance signal resolution with data processing efficiency. Afterwards, the GoPro video records were cross-referenced with the CWT data to identify potential AE events for further analysis.

AE events, summarized in **Table 2**, were selected based on the following AE characteristics: notable impulses detected and frequencies typically ranging from 20 to 500 kHz. As shown in the table below, with the testing speed increased, the AE events detected also increased accordingly, which indicated that higher speeds would increase more. The defect developments were due to higher dynamic loads, which resulted in AE events. Additionally, these signals were confirmed with video records that wheel-rail impacts generated them.

**Table 2.** Summary of AE events in RDTF loop.

Test Location	Test Speed (MPH)	AE Events Amount	Total
RDTF	5	12, 10, 11, 17, 9	59
	10	14, 10, 11, 15, 17	67
	15	23, 15, 19, 11, 15	83
	20	22, 25, 16, 20, 22 17, 24, 18, 21, 19	204

**Figure 13** presents the CWT of typical impulse signals from different testing speeds involving complicated frequency distributions. While these signals generally lasted very short, the frequency range was typically distributed from 60 to 500

kHz across the tested speeds. Meanwhile, the wave energy was primarily concentrated in the 60 - 150 kHz range, and a notable amount of energy was observed in the 200 - 300 kHz range. These findings are aligned with the conclusions of the first stage field test in Nevada.

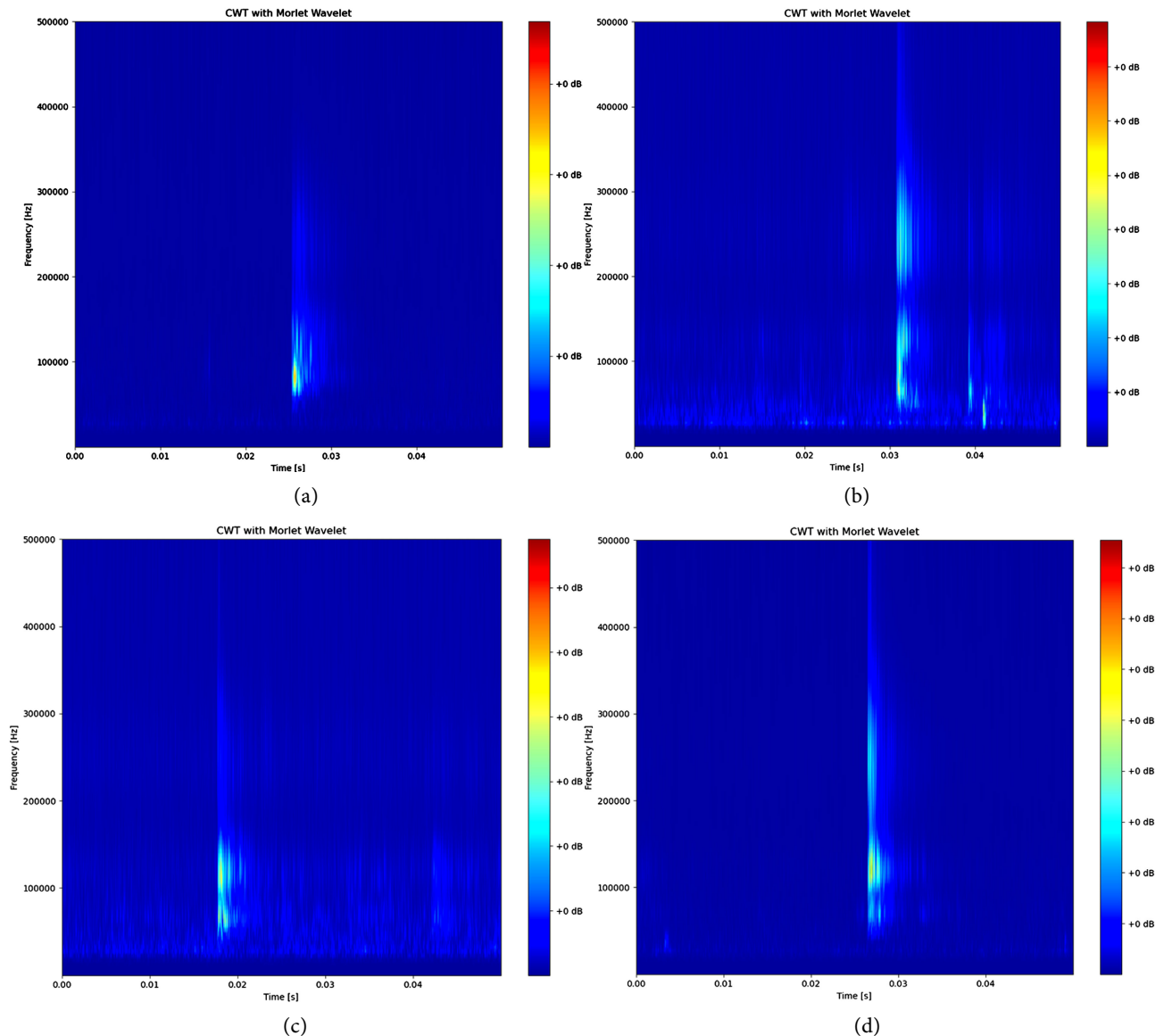


**Figure 13.** AE signals in RDTF tests: (a) 5 mph; (b) 10 mph; (c) 15 mph; (d) 20 mph.

**Figure 14** presents the time-frequency plots of ambient noise across four testing speeds, where the energy was primarily concentrated below 150 kHz, a clear distinction from the defect-induced AE signals. Ambient noise, compared to the impulse signals, is characterized by relatively low frequency, continuity, and randomness. This observation is consistent with findings from the initial stage of the field test in Nevada. Further analysis was conducted with a narrower time scale to examine the time-frequency characteristics, as shown in **Figure 15**. This figure represents a typ-

ical AE pattern for events collected during the test. It is interesting to note that the signal did not exhibit significant attenuation during the impulse period. However, given the defect density within this loop, the number of detected events was relatively low. Two factors may have contributed to this: firstly, the testing vehicle was a hi-rail vehicle modified from a pickup truck, resulting in a significantly lower axial load than a commercial hopper. Secondly, all defects in the loop were artificially induced through cutting or drilling, which may have stabilized these defects, preventing further development under low compression conditions.

Based on these findings, it is essential to analyze the data collected from the HTL loop and compare the characteristics of artificial defects with those of natural defects. Additionally, the comparison should extend to the rate of AE events occurring with the commercial hopper.

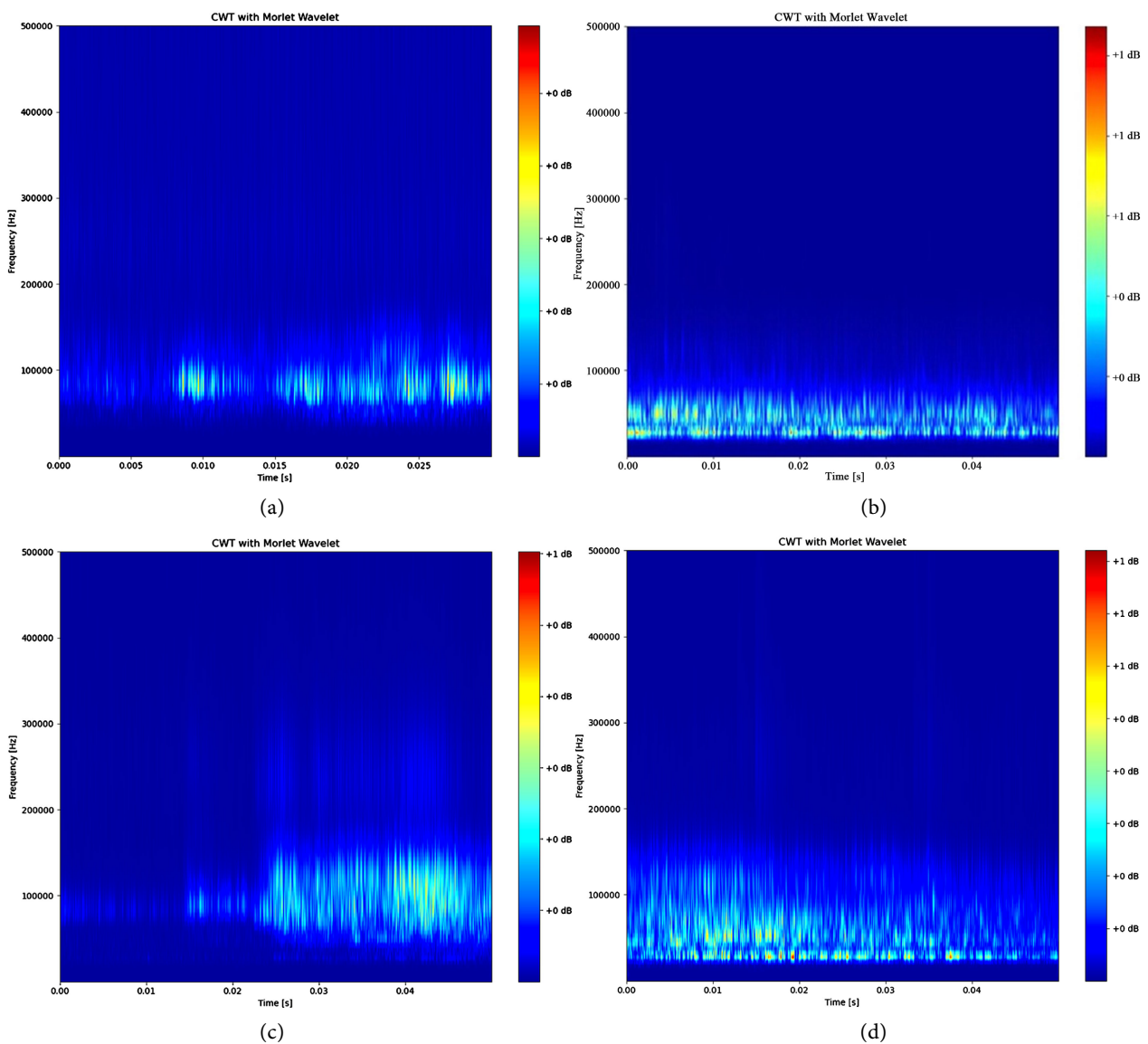


**Figure 14.** Ambient noise signals in RDTF tests.

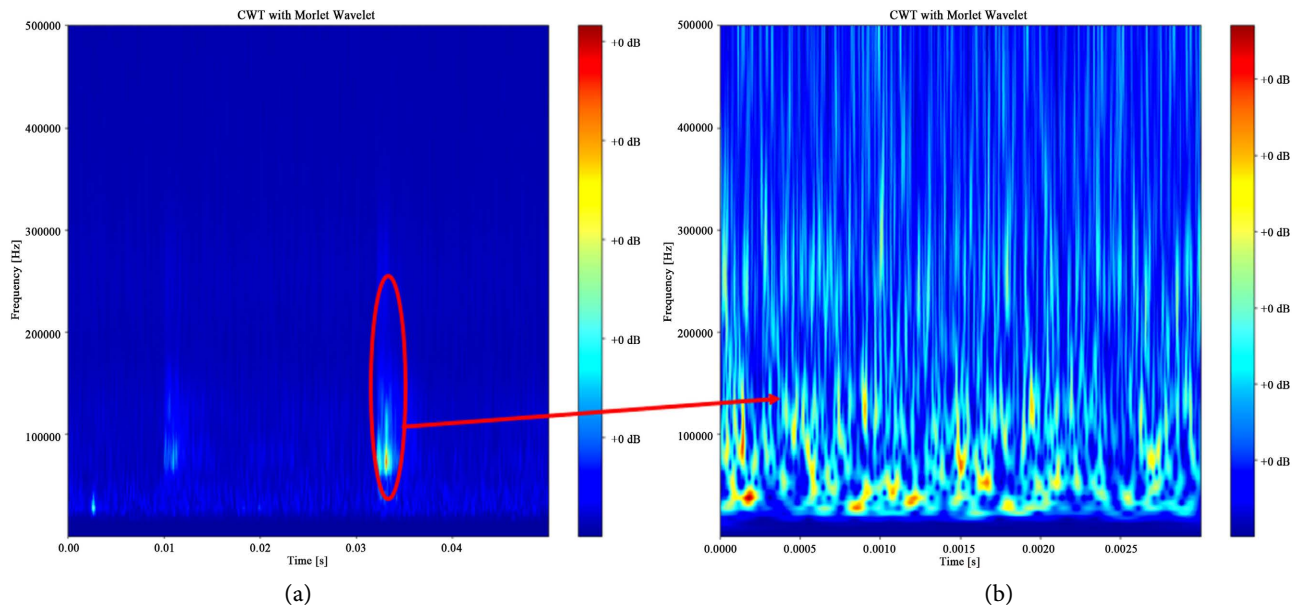


**Figure 15.** CWT of impulse signals: (a) overview; (b) narrower time window.

### 4.3. Time-Frequency Analysis of HTL Loop

As with the RDTF test, time-frequency analysis was performed to evaluate the AE characteristics of naturally generated defects on HTL, using the CWT with a 20 kHz high-pass filter. The CWT analysis was cross validated using the same methods applied to the RDTF data. Specifically, the time window for CWT analysis was set to 0.05 seconds, and GoPro video recordings were validated with the CWT data to identify potential AE events. A total of 31 defects were analyzed from the tests on the HTL Loop.

Unfortunately, the CWT features observed from different defects showed significant variations in certain defect area plots. Some plots clearly identified AE characteristics, as shown in **Figure 16**, where a distinct AE impulse is visible with a major energy distribution between 20 - 90 kHz along with a notable high frequency range from 120 kHz to 500 kHz. However, other plots presented more complex patterns. In many defect areas, multiple AE-like impulses were observed throughout the defect regions (**Figure 17**). These impulses also appeared in non-defect areas, complicating the identification of AE signals. When the analysis was conducted on a narrower time scale, the signals exhibited continuous features, making it challenging to distinguish AE characteristics.

In response to this challenge, this project used ML techniques to study the complexity of identifying AE features in these intricate scenarios. Such advanced analytical tools could enable the automated extraction and classification of AE signals from extensive datasets. The ML models were trained using the data from the HTL field tests, attempting to learn the characteristics of AE signals associated with different defect types and conditions. The application of ML in this context represents a significant advancement in the analysis of AE signals contributing to more efficient and reliable rail defect detection methods in future studies.

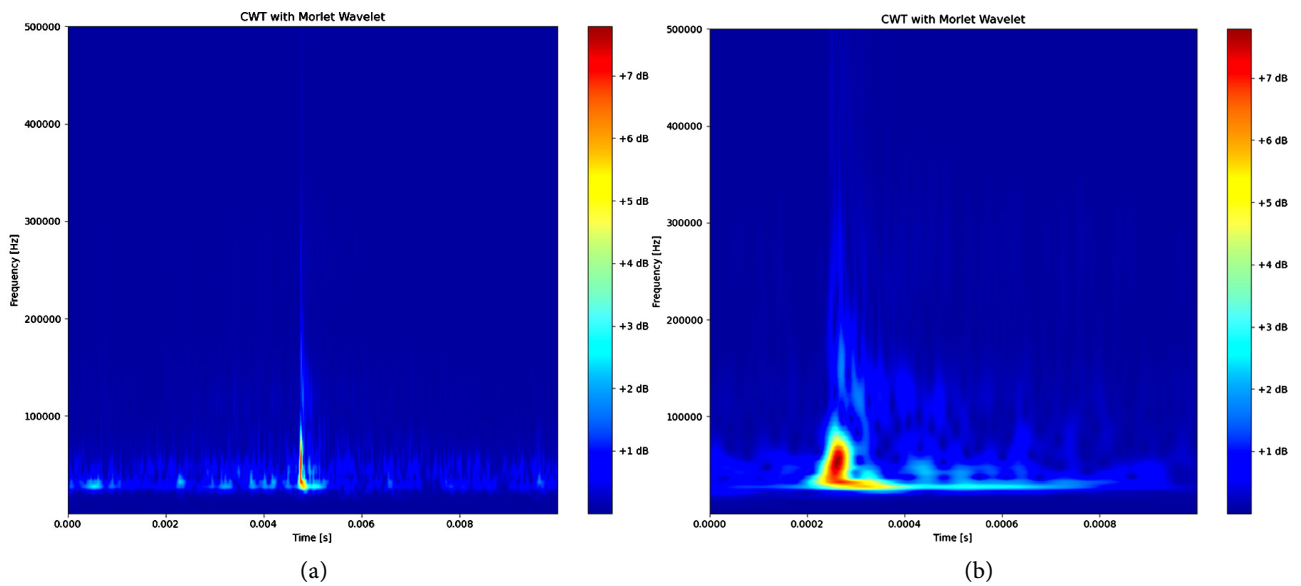


**Figure 16.** Visible AE signal detected in HTL loop.

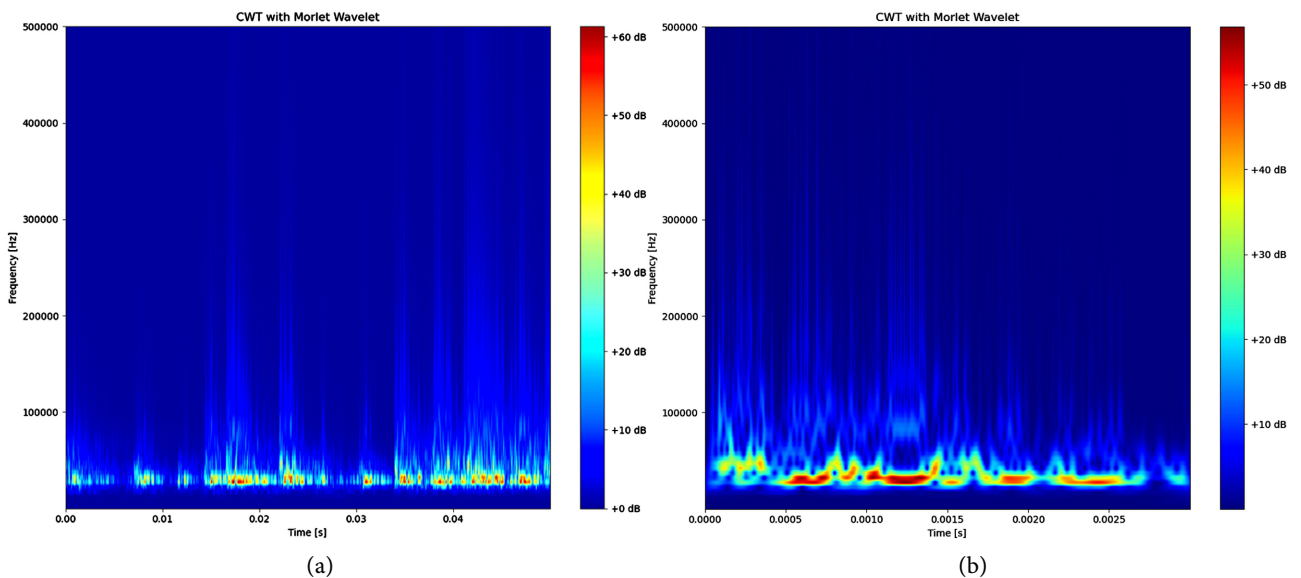


**Figure 17.** Ambient noise affected signals in HTL loop.

#### 4.4. Machine Learning Analysis in Defect Analysis

Considering the challenges of managing large datasets characterized by complicated noise interference in real-world data analysis, traditional methods often fall short in efficiently classifying such complex data. To address this problem, ML algorithms, such as artificial neural networks (ANNs), support vector machines (SVMs), and relevance vector machines (RVMs), have been widely adopted for fault diagnosis and damage detection [19]. In recent years, convolutional neural networks (CNNs) have demonstrated exceptional capabilities in handling intricate, high-dimensional data [20].

CNNs are designed to automatically and adaptively learn the grid-like topology

of datasets, such as images or time-series data, through multiple layers of processing. Their architecture, which includes convolutional layers, pooling layers, and fully connected layers, allows them to capture complex patterns while reducing computational costs through parameter sharing and dimensionality reduction. CNNs have proven to be highly successful in a wide range of applications, including image detection, segmentation, and pattern recognition. In the context of structural damage detection, CNNs have been used to analyze visual images, vibration signals, and AE signals with remarkable accuracy. Their ability to process and interpret AE signals' spatial and temporal features makes CNNs especially suited for identifying subtle patterns that may indicate the presence of defects.

In the following chapter, we will utilize CNNs to process two-dimensional representations of time-series data; we aim to improve the robustness and reliability of our defect detection approach, ultimately contributing to more efficient and accurate railway maintenance and safety protocols.

#### **4.4.1. CNN Model for AE Classification**

The application of CNNs, which is traced back as early as 1998 [21], has revolutionized various fields, including activity recognition, sentence classification, text recognition, face recognition, object detection, image characterization, and more. The power of CNNs lies in their unique architecture, which mimics the visual cortex's processing of visual stimulations. This makes CNNs particularly effective for high-dimensional data such as images and videos. A typical CNN architecture consists of several layers, including convolutional layers, pooling layers, and fully connected layers, each playing a crucial role in the network's ability to learn and generalize from data.

The CNN model employed in this study is custom designed to accommodate various needs, such as dataset variations and CNN dimension modifications. In past research, CWT plots were utilized as data inputs for CNN analysis [20], which converted acoustic datasets into image datasets. However, the resolution and plotting method of the images significantly influenced the outcome of CNN models. In this study, Mel Frequency Cepstral Coefficients (MFCCs) and their deltas were introduced to extract the features of datasets and utilized as input datasets. MFCCs represent the short-term power spectrum of a sound signal commonly used in acoustic processing. They are derived by taking the Fourier transform of a signal, mapping the powers of the spectrum onto the Mel scale, and then applying a logarithm transformation, followed by the inverse Fourier transform. The resulting coefficients provide a compact and perceptually relevant acoustic signal representation. The deltas of MFCCs, also known as delta coefficients, capture temporal dynamics by calculating the difference between consecutive MFCCs. Such delta coefficients provide additional information about how the acoustic features change over time, enhancing the ability to recognize patterns in acoustic signals. MFCCs and their deltas are commonly used as features in machine learning models for tasks like speech recognition and audio classification.

In this study, the model took MFCCs and deltas as input, initially structured into  $256 \times 98 \times 2$ , where 256 represents the number of Mel bands, 98 is the number of frames, and two channels denote the original MFCCs and their delta values. The architecture comprised multiple convolutional layers with batch normalization and ReLU activation functions to ensure stable and efficient learning, as shown in **Figure 18**. The convolutional layers progressively extract features from the input data, with the layers and the subsequent layers using various filter setups, with the consideration of optimizing the classification rate. The kernel size was set to  $3 \times 3$ . Max pooling layers with a pool size of  $2 \times 2$  followed each convolutional layer, reducing the spatial dimensions of the feature maps while retaining the most salient information. A global max pooling layer was incorporated to condense the feature maps further, followed by fully connected layers. The first dense layer had 16 units with ReLU activation, and the output layer consisted of 2 units with SoftMax activation, corresponding to the two classes in the classification task. The model was compiled with the Adam optimizer, using a learning rate  $1e-4$ , and trained with the sparse categorical cross-entropy loss function, with accuracy as the primary evaluation metric. To ensure robust performance, the model undergoes K-fold cross-validation, allowing it to be trained and validated on different data splits, providing a comprehensive evaluation of its classification capabilities. However, the data structures were modified to optimize the training performance, including revising the layer numbers, input structure, and layer filter amount.

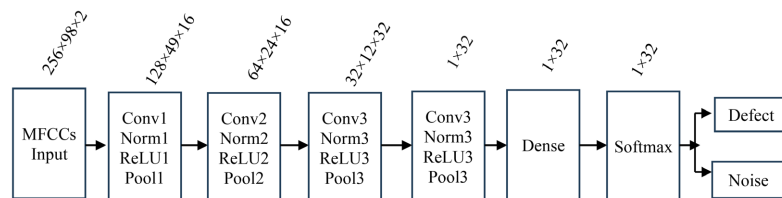


**Figure 18.** General architecture for defect classification.

#### 4.4.2. Training Process and Results

The datasets used in the training consist of potential AE signals extracted from defect locations from the HTL loop tests and non-AE signals, including ambient noise and impulse-like mechanical vibrations, extracted from non-defect areas. Like before, a preliminary time window of 0.05 seconds was initially employed for data processing. However, to accurately label the datasets for the CNN model, it is essential to determine an appropriate time window length that captures AE signal components while excluding unrelated signal components.

Basic setups for the used devices in relation to parameters used in analysis are as follows. The GoPro frame rate was set to 60 Hz at its highest resolution, with an error margin of  $\pm 0.017$  seconds. Additionally, the defect zone was set at 15 inches—a value deemed appropriate based on information from TTCI and considering the maximum testing speed of 40 mph, corresponding to a passing time of 0.02 seconds. Consequently, a minimum time window length of 0.054 seconds was determined for the datasets. To ensure that all AE signal components were

captured, the time window was finally doubled to 0.11 seconds.

The AE signal datasets were selected through initial visual inspection, focusing on those exhibiting significant AE characteristics or those combined with ambient noise. As previously mentioned, data from the three identical sensors were used in the analysis. Consequently, the total number of datasets extracted from defect areas, regardless of whether AE signals were detected, was  $31 \text{ defects per run} \times 12 \text{ runs} \times 3 \text{ sensor sets} = 1,116$ . Additionally, noise datasets were extracted from noisy areas, resulting in a total of  $756 \times 3 = 2,268$  samples. To start with the training, the dataset was set up as explained in the previous chapter; each CNN model utilized K-fold cross-validation (with  $K = 7$ ) to ensure robustness and minimize overfitting.

In the initial trials, two configurations of convolutional layers and dataset sizes were evaluated:  $8 \times 8 \times 16 \times 16$  for the first setup and  $16 \times 16 \times 32 \times 64$  for the second. In both configurations, 1,116 samples were utilized as defect datasets, and 2,268 samples were employed as noise datasets. As shown in **Table 3**, the  $8 \times 8 \times 16 \times 16$  setup exhibited consistently low-test accuracy and training accuracy, suggesting that this simpler architecture may not effectively capture the necessary features for the datasets in this analysis. In contrast, the  $16 \times 16 \times 32 \times 64$  architecture achieved higher training accuracy and lower training loss, indicating better model fitting. However, the test accuracy showed fluctuations, suggesting potential overfitting issues or poor-quality data in the sets. Therefore, as an effort to improve the quality of training data and enhance model's generalization, data lacking significant AE patterns was removed from the training.

**Table 3.** Training results with full datasets.

Conditions	Defect samples	Noise samples	Layers	Training accuracy	Training loss	Test accuracy	F1 score
All the data in defect zone	1116	2268	$8 * 8 * 16 * 16$	0.771	0.486	0.693	0.356
				0.791	0.449	0.741	0.42
				0.785	0.453	0.708	0.492
				0.79	0.471	0.703	0.388
				0.822	0.394	0.693	0.519
				0.793	0.448	0.651	0.412
All the data in defect zone	1116	2268	$16 * 16 * 32 * 64$	0.819	0.394	0.571	0.455
				0.959	0.21	0.73	0.54
				0.97	0.22	0.77	0.53
				0.96	0.2	0.69	0.34
				0.96	0.18	0.82	0.68
				0.94	0.23	0.67	0.55
				0.94	0.2	0.64	0.51
				0.96	0.19	0.56	0.49

In **Table 4**, around 25% of the poor-quality data was removed from the defect dataset, and the same portion of the noise data was removed from the noise dataset randomly to maintain the data proportions the same as before. In this follow-up

analysis, both configurations ( $8 \times 8 \times 16 \times 16$  and  $16 \times 16 \times 32 \times 64$ ) were re-evaluated using datasets that included only potential AE data.

Compared with the previous setup, which included all data from defect zones, this refined dataset increased model performance in both configurations. For the  $8 \times 8 \times 16 \times 16$  configuration, the test accuracy showed a significant increase, particularly reaching 84% one-fold, with the F1 score also improving to a maximum of 0.716, which is promising. This suggests that even simpler architectures can achieve better generalization when data quality is improved by filtering out irrelevant data. Conversely, the  $16 \times 16 \times 32 \times 64$  configuration showed signs of overfitting, with high training accuracy but less consistent test accuracy, along with fluctuations in performance. Although there were some improvements in the F1 score, reaching up to 0.6, the overfitting suggests that more complex architectures may not necessarily improve precision or generalization.

However, while the refinement of data improved performance, the overall test accuracy still remained lower than expected, indicating that further improvements in defect data quality are necessary for achieving higher accuracies. This highlights that simply removing bad data might not be sufficient; enhancing the overall quality and relevance of defect data is crucial for better model performance.

**Table 4.** Training results with potential AE data only.

Conditions	Defect samples	Noise samples	Layers	Training accuracy	Training loss	Test accuracy	F1 score
Potential AE data only	831	1671	$8 * 8 * 16 * 16$	0.865	0.292	0.7	0.475
				0.97	0.15	0.72	0.453
				0.97	0.136	0.49	0.485
				0.965	0.148	0.73	0.417
				0.94	0.21	0.84	0.691
				0.98	0.13	0.78	0.716
				0.99	0.11	0.76	0.725
Potential AE data only	831	1671	$16 * 16 * 32 * 64$	0.99	0.09	0.73	0.57
				0.99	0.11	0.78	0.6
				0.98	0.17	0.75	0.61
				0.99	0.11	0.73	0.37
				0.98	0.16	0.72	0.51
				0.97	0.16	0.7	0.54
				0.99	0.1	0.58	0.42

For further enhancement, this project separated the internal defects (transverse defects) and external defects (surface defects) into two distinct datasets. These datasets were then fed into the model separately to determine whether the accuracy results would improve with higher clarity in provided defect data. Out of the 831 defect samples presented in **Table 4**, 399 data samples were categorized as internal defects and the remaining 432 were designated as external defects.

Initially, the layers were set as  $8 \times 8 \times 16 \times 16$  to possibly avoid overfitting or underfitting. As shown in **Table 5**, the results for the internal defects (transverse

defects) indicated a range of test accuracies from 0.55 to 0.71, with corresponding F1 scores ranging from 0.09 to 0.36. The training accuracy varied between 0.73 and 0.78, while the training loss was relatively stable, ranging from 0.47 to 0.53. Despite some improvement in test accuracy, the F1 scores suggest that the model's ability to balance precision and recall was still limited. As to the external defects (surface defects), the results show a similar trend, with test accuracies ranging from 0.57 to 0.66 and F1 scores between 0.03 and 0.24. The training accuracy was slightly higher, reaching 0.82, with training loss decreasing to as low as 0.45. However, the lower F1 scores indicate that while the model was able to achieve better training accuracy, it still failed to properly classify all the defects and noises properly.

**Table 5.** Training results with internal (a) and external (b) defects only.

(a)							
Conditions	Defect samples	Noise samples	Layers	Training accuracy	Training loss	Test accuracy	F1 score
Transverse defects only	399	798	8 * 8 * 16 * 16	0.73	0.53	0.67	0.17
				0.74	0.52	0.66	0.19
				0.77	0.5	0.63	0.29
				0.76	0.5	0.71	0.36
				0.74	0.52	0.64	0.14
				0.76	0.5	0.64	0.26
				0.78	0.47	0.55	0.09
(b)							
Conditions	Defect samples	Noise samples	Layers	Training accuracy	Training loss	Test accuracy	F1 score
Transverse defects only	432	864	8 * 8 * 16 * 16	0.73	0.54	0.66	0.15
				0.79	0.5	0.65	0.24
				0.76	0.53	0.65	0.03
				0.74	0.53	0.64	0.18
				0.76	0.51	0.64	0.08
				0.82	0.45	0.59	0.21
				0.76	0.5	0.57	0.15

These results suggest that separating the defects into internal and external categories did not lead to significant improvements in the model performance, particularly in terms of the F1 score, which remained low in both cases. After such attempts, no significant improvement in overall performance was observed, and the quality of the raw data collected in the field tests was necessary to be validated.

#### 4.5. Additional Tests to Validate Data Quality

The tests that have been conducted so far emphasized the importance of data quality, leading to several critical questions with respect to system capability to collect quality data and adequateness of system deployment, which mounts sensors onto a train frame as a non-contact method. In fundamental investigations into these aspects, additional tests were designed. A series of pencil lead break (PLB) tests

were conducted both in the lab and in the field. The PLB test is also known as the Hsu-Nielsen test, is commonly employed to replicate AE signals by breaking the tip of a pencil lead against the material surface. As the pencil lead in a specially designed pencil breaks, an elastic wave can be generated as a result of the sudden stress release. The ASTM E976-15 [22] recommends using a mechanical pencil with 2H leads of 0.5 mm diameter as the AE source for reliable results. Each lead to be broken was approximately 3 mm in length. The Nielsen shoe is used to position the pencil lead correctly towards the testing materials at a 30° angle (Figure 19). Researchers adopted PLB as a simulation tool to produce AE signals and investigate the acoustic features of AE signals.

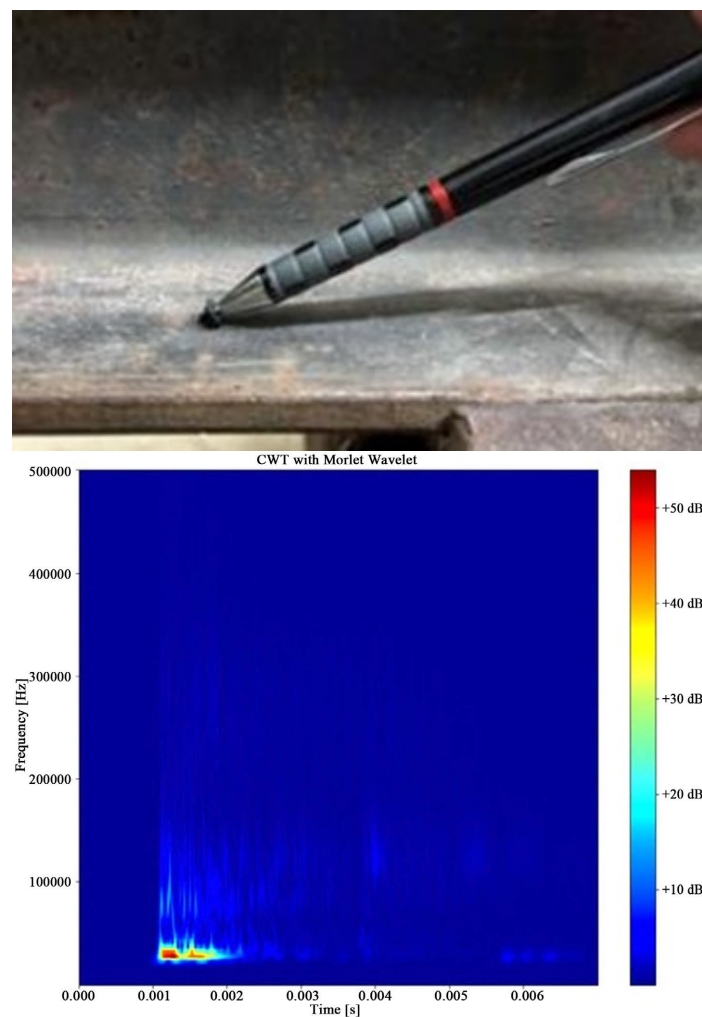


**Figure 19.** PLB test and time-frequency analysis.

The first question focused on whether the detection prototype was properly configured to receive AE signals. To evaluate the system setup and ensure the prototype's ability to capture acoustic signals accurately, a PLB test was made with sensors attached to the surface of a steel plate. The results from this test were positive, with the time-frequency analysis clearly indicating successful detection of

the PLB signals (**Figure 19**).

The second question aimed to determine whether AE signals generated in the rail could be effectively captured by sensors mounted on the train frame. For this evaluation, a field test was conducted at the Nevada Railroad Museum. Sensors were installed at various locations on the wheel and suspension frame, and PLB tests were performed multiple times under the rail head to simulate AE signal generation. These tests were designed to verify if the AE signals could propagate through the rail into the wheel and be detected by the sensors. However, the results from the second test were discouraging, with all sensor locations failing to capture the AE signals properly. The tests were repeated multiple times at various sensors to verify the outcome. In all cases, the PLB signals were not properly detected by the sensors, regardless of their installation positions.

This consistent failure suggests that the AE signals were unable to propagate through the rail into the wheel without proper coupling. AE signals are highly dependent on the medium they propagate through, and any discontinuity at the interface between different materials can lead to significant signal attenuation. In this case, the rail and train frame presented multiple medium changes, including metal-to-metal and metal-to-air interfaces, which caused significant energy loss during propagation.

Based on these findings, it can be concluded that the acoustic signals collected in previous tests at the TTCI and the Nevada Railroad Museum did not originate from the rails but from the train itself. These signals were likely mechanical vibrations that presented similar patterns of AE signals, which explains the consistently low performance of the machine learning model. Given that the bone-conduct sensors cannot capture AE signals when installed on trains, it is necessary to explore alternative methods for collecting acoustic signals that do not suffer from propagation issues. This exploration is critical to improving the capability of AE signal detection in field applications.

## 5. Discussion and Conclusion

This study explored the feasibility of on-vehicle AE detection for rail defect detection using bone-conduct sensors. CWT analysis and machine learning were employed to identify AE characteristics. Key findings revealed several limitations in this approach, indicating the need for significant advancements in AE-based rail health monitoring.

1) Signal Detection and Analysis Challenges: The CWT analysis and machine learning models failed to identify AE features of rail defects. Despite testing across multiple defect types and speeds, the AE characteristics essential for reliable defect detection were not consistently detected, indicating limitations in current data processing methods for in-motion applications.

2) Propagation Limitations: Further investigations using PLB tests presented that AE signals generated by rail defects failed to propagate from the rail through the wheel and into the sensors. This finding indicated a fundamental limitation in

using contact-based methods for defect detection, as AE signals attenuate significantly before reaching vehicle-mounted sensors.

3) Implications of Findings: The findings indicate a critical limitation for on-vehicle AE detection: ensuring effective AE signal propagation. In this research, the inability of AE signals to propagate across different media due to insufficient coupling led to the failure to detect rail defects. To address this challenge, two approaches are recommended: (1) improving the coupling between the media to facilitate uninterrupted AE signal transmission, and (2) adopting non-contact techniques for AE signal collection to eliminate the need for signal propagation through multiple media, thereby preserving signal integrity.

4) Future Recommendations for Non-Contact AE Detection: Given the challenges with contact-based AE signal transmission, the results suggest that effective on-vehicle rail defect inspection requires the development of non-contact AE detection methods. Non-contact approaches, such as air-coupled sensors, may enable non-contact AE signal detection without physical contact between the vehicle and the rail, addressing the signal propagation challenge in this research.

In conclusion, while on-vehicle AE detection shows promise for automated rail health monitoring, this study illustrates the limitations of contact-based approaches and emphasizes the potential of non-contact technologies for addressing these challenges. Future research should focus on refining non-contact detection methods and improving signal processing algorithms to realize reliable, high-speed rail defect inspection.

## Acknowledgements

This study was supported by the Tier 1 University Transportation Center on Improving Rail Transportation Infrastructure Sustainability and Durability at the University of Nevada Las Vegas.

## Conflicts of Interest

The authors declare no conflicts of interest regarding the publication of this paper.

## References

- [1] Li, Q. and Ren, S. (2012) A Real-Time Visual Inspection System for Discrete Surface Defects of Rail Heads. *IEEE Transactions on Instrumentation and Measurement*, **61**, 2189-2199. <https://doi.org/10.1109/tim.2012.2184959>
- [2] Deutschl, E., Gasser, C., Niel, A. and Werschonig, J. (2004) Defect Detection on Rail Surfaces by a Vision Based System. *IEEE Intelligent Vehicles Symposium*, 2004, Parma, 14-17 June 2004, 507-511. <https://doi.org/10.1109/ivs.2004.1336435>
- [3] Bojarczak, P. (2013) Visual Algorithms for Automatic Detection of Squat Flaws in Railway Rails. *Insight—Non-Destructive Testing and Condition Monitoring*, **55**, 353-359. <https://doi.org/10.1784/insi.2012.55.7.353>
- [4] He, Z., Wang, Y., Yin, F. and Liu, J. (2016) Surface Defect Detection for High-Speed Rails Using an Inverse P-M Diffusion Model. *Sensor Review*, **36**, 86-97. <https://doi.org/10.1108/sr-03-2015-0039>

- [5] Xiong, Z., Li, Q., Mao, Q. and Zou, Q. (2017) A 3D Laser Profiling System for Rail Surface Defect Detection. *Sensors*, **17**, Article 1791. <https://doi.org/10.3390/s17081791>
- [6] Office of Railroad Policy and Development (2011) Rolling Contact Fatigue: A Comprehensive Review.
- [7] Lanza di Scalea, F., Rizzo, P., Coccia, S., Bartoli, I., Fateh, M., Viola, E., et al. (2005) Non-contact Ultrasonic Inspection of Rails and Signal Processing for Automatic Defect Detection and Classification. *Insight—Non-Destructive Testing and Condition Monitoring*, **47**, 346-353. <https://doi.org/10.1784/insi.47.6.346.66449>
- [8] Rizzo, P. and Coccia, S. (2009) Noncontact Rail Monitoring by Ultrasonic Guided Waves. *Encyclopedia of Structural Health Monitoring* 2397.
- [9] Mariani, S., Nguyen, T., Zhu, X. and Lanza di Scalea, F. (2017) Field Test Performance of Noncontact Ultrasonic Rail Inspection System. *Journal of Transportation Engineering, Part A: Systems*, **143**. <https://doi.org/10.1061/jtepbs.0000026>
- [10] Kim, N., Sohn, H. and Han, S. (2012) Rail Inspection Using Noncontact Laser Ultrasonics. *Journal of the Korean Society for Nondestructive Testing*, **32**, 696-702. <https://doi.org/10.7779/jksnt.2012.32.6.696>
- [11] Lanza di Scalea, F., Zhu, X., Capriotti, M., Liang, A.Y., Mariani, S. and Sternini, S. (2017) Passive Extraction of Dynamic Transfer Function from Arbitrary Ambient Excitations: Application to High-Speed Rail Inspection from Wheel-Generated Waves. *Journal of Nondestructive Evaluation, Diagnostics and Prognostics of Engineering Systems*, **1**, Article ID: 011005. <https://doi.org/10.1115/1.4037517>
- [12] Coccia, S., Bartoli, I., Marzani, A., Lanza di Scalea, F., Salamone, S. and Fateh, M. (2011) Numerical and Experimental Study of Guided Waves for Detection of Defects in the Rail Head. *NDT & E International*, **44**, 93-100. <https://doi.org/10.1016/j.ndteint.2010.09.011>
- [13] Coccia, S., Phillips, R., Nucera, C., Bartoli, I., Salamone, S., Lanza di Scalea, F., et al. (2011) UCSD/FRA Non-Contact Ultrasonic Guided-Wave System for Rail Inspection: An Update. *SPIE Proceedings*, **7981**, Article ID: 798113. <https://doi.org/10.1117/12.880238>
- [14] Bruzelius, K. and Mba, D. (2004) An Initial Investigation on the Potential Applicability of Acoustic Emission to Rail Track Fault Detection. *NDT & E International*, **37**, 507-516. <https://doi.org/10.1016/j.ndteint.2004.02.001>
- [15] Nivesrangsan, P., Steel, J.A. and Reuben, R.L. (2007) Source Location of Acoustic Emission in Diesel Engines. *Mechanical Systems and Signal Processing*, **21**, 1103-1114. <https://doi.org/10.1016/j.ymsp.2005.12.010>
- [16] Huang, M., Jiang, L., Liaw, P. and Brooks, C. (1998) Using Acoustic Emission in Fatigue and Fracture Materials Research. *JOM*, **50**, 1-12.
- [17] Zhang, X., Feng, N., Wang, Y. and Shen, Y. (2015) Acoustic Emission Detection of Rail Defect Based on Wavelet Transform and Shannon Entropy. *Journal of Sound and Vibration*, **339**, 419-432. <https://doi.org/10.1016/j.jsv.2014.11.021>
- [18] Zumpano, G. and Meo, M. (2006) A New Damage Detection Technique Based on Wave Propagation for Rails. *International Journal of Solids and Structures*, **43**, 1023-1046. <https://doi.org/10.1016/j.ijsolstr.2005.05.006>
- [19] de Oliveira, R. and Marques, A.T. (2008) Health Monitoring of FRP Using Acoustic Emission and Artificial Neural Networks. *Computers & Structures*, **86**, 367-373. <https://doi.org/10.1016/j.compstruc.2007.02.015>
- [20] Li, D., Wang, Y., Yan, W. and Ren, W. (2020) Acoustic Emission Wave Classification

- for Rail Crack Monitoring Based on Synchrosqueezed Wavelet Transform and Multi-Branch Convolutional Neural Network. *Structural Health Monitoring*, **20**, 1563-1582. <https://doi.org/10.1177/1475921720922797>
- [21] Lecun, Y., Bottou, L., Bengio, Y. and Haffner, P. (1998) Gradient-Based Learning Applied to Document Recognition. *Proceedings of the IEEE*, **86**, 2278-2324. <https://doi.org/10.1109/5.726791>
- [22] ASTM E976-15 (1993) Standard Guide for Determining the Reproducibility of Acoustic Emission Sensor Response. ASTM Book of Standards.